

Structural phase transition and magnetism in hexagonal  $\text{SrMnO}_3$ 

A. Daoud-Aladine,<sup>1</sup> C. Martin,<sup>2,1</sup> L. C. Chapon,<sup>1</sup> M. Hervieu,<sup>2</sup> K. S. Knight,<sup>1</sup> M. Brunelli,<sup>3</sup> and P. G. Radaelli<sup>1,4</sup>

<sup>1</sup>ISIS facility, Rutherford Appleton Laboratory-CCLRC,  
Chilton, Didcot, Oxfordshire, OX11 0QX, United Kingdom.

<sup>2</sup>Laboratoire CRISMAT-UMR, 6508 ENSICAEN,  
6, Marechal Juin, 14050 Caen, France

<sup>3</sup>European Synchrotron Radiation Facility,  
BP 220, F-38043 Grenoble Cedex, France

<sup>4</sup>Dept. of Physics and Astronomy,  
University College London, Gower Street,  
London WC1E 6BT, United Kingdom

(Dated: March 23, 2024)

## Abstract

The structural and magnetic properties of the hexagonal four-layer form of  $\text{SrMnO}_3$  have been investigated by combining magnetization measurements, electron diffraction and high-resolution synchrotron X-ray and neutron powder diffraction. Below 350K, there is subtle structural phase transition from hexagonal symmetry (space group  $P6_3/mmc$ ) to orthorhombic symmetry (space group  $C222_1$ ) where the hexagonal metric is preserved. The second-order phase transition involves a slight tilting of the corner-sharing  $\text{Mn}_2\text{O}_9$  units composed of 2 face-sharing  $\text{MnO}_6$  octahedra and the associated displacement of  $\text{Sr}^{2+}$  cations. The phase transition is described in terms of symmetry-adapted displacement modes of the high symmetry phase. Upon further cooling, long range magnetic order with propagation vector  $\mathbf{k} = (0;0;0)$  sets in below 300K. The antiferromagnetic structure, analyzed using representation theory, shows a considerably reduced magnetic moment indicating the crucial role played by direct exchange between Mn centers of the  $\text{Mn}_2\text{O}_9$  units.

PACS numbers: 61.12.-q, 61.14.-x, 61.10.-i, 75.47.Lx, 75.00.00

## I. INTRODUCTION

Transition metal oxides show remarkable physical properties, such as colossal magnetoresistance in manganites<sup>1</sup>, or superconductivity in cuprates<sup>2</sup>, which after decades of researches, remain only partly understood. This reflects our understanding of the structural, electronic and magnetic phenomena, which is well established only in the limit where the systems show localized or itinerant electron behavior<sup>3</sup>. Doping with electrons or holes is the canonical method to explore the intermediate regime. For example, in  $R_{1-x}D_xMnO_3$  manganite perovskites ( $R$ : trivalent cation,  $D$ : divalent cation), the Mn valence is formally intermediate  $3+x$ , affecting the electrical conductivity and leading to a complex phase diagram.

However, even undoped compounds display an intriguing evolution of their magnetic properties as the geometry and coordination are changed. For example, in the  $RMnO_3$  and  $DMnO_3$  end members of the  $R_{1-x}D_xMnO_3$  series, Mn has undoubtedly well localized electrons, making these compounds prototype antiferromagnetic (AF) Mott insulators. Their magnetic properties fit a Heisenberg picture, in which superexchange (SE) interactions couple high spin  $Mn^{3+}$  ( $S = 2$ ) and  $Mn^{4+}$  ( $S = 3/2$ ) ions at  $x = 0$  and  $x = 1$  respectively<sup>4,5,6</sup>. This can be contrasted to the very unusual magnetic properties of some hexagonal manganite halides containing single valent Mn ions.  $CsMnBr_3$ <sup>7</sup> and  $CsMnI_3$ <sup>8</sup> compounds containing  $S = 5/2$  high spin  $Mn^{2+}$  ions arranged in infinite strings of face-sharing  $MnO_6$  octahedra parallel to the  $c$  axis, from which exchange frustration is expected between the direct and the super-exchange interactions of different sign within the chains. Exchange frustration in the basal plane also brings about chirality of the magnetic state and a spin dynamic corresponding to new universality classes<sup>7</sup>. One may be tempted to conclude that these unusual magnetic properties arise from the quasi-one-dimensional nature of the exchange, combined with easy axis anisotropy. However, isostructural  $BaMnO_3$  ( $S = 3/2$ ) does not show such effects, but it has instead a simple antiferromagnetic structure and rather classical magnetic behavior with the ordered moment value saturating at low temperatures<sup>9</sup>.

In order to separate the influence upon the magnetic properties of the lattice geometry from more conventional chemical effects, the study of polymorphic compounds, which display different stable or metastable structures with the same chemical composition is particularly valuable. As discussed by Nagas and Roth<sup>10</sup>, the stability of the structures adopted by  $ABX_3$  compounds depends on the tolerance factor  $t = \frac{r_A + r_X}{\sqrt{2}(r_B + r_X)}$ , where  $r_A$

is the average ionic radius of the A-site cations, while  $r_B$  and  $r_X$  are those of the B-site metal and of the anion (oxygen, halogen or chalcogen). Most manganites have  $t \approx 1$ , and crystallize in orthorhombic or rhombohedral perovskite structures showing cooperative tilting of the corner sharing  $MO_6$  array, with respect to the ideal cubic perovskite. For sufficiently large  $r_A$ ,  $t > 1$  materials adopt a different hexagonal symmetry, as in the case of  $BaMO_3$  and the aforementioned halides. For  $t > 1$ , polytypes are obtained depending on the synthesis procedure<sup>10,11</sup>. These polytypes are characterized by the stacking sequence of the  $AO_3$  layers, which controls how the  $MO_6$  octahedra arrange. Octahedra are sharing corners across the central  $AO_3$  layer of *..abc..* sequences, while they share faces across *..aba..* type sequences.

For example, synthesized at ambient pressure in air,  $SrMO_3$  ( $t = 1.05$ ) has a four layer (4L) abac stacking sequence of  $SrO_3$  layers as shown in Fig.1, whereas modified synthesis routines are required to obtain the cubic perovskite<sup>12</sup>. 4L is a rather rare polytype among  $ABX_3$  compounds, and represents an intermediate case between the hexagonal (2L) polytype adopted by  $BaMO_3$ , and the familiar perovskite structure of  $CaMO_3$  containing only corner sharing octahedra. It is therefore interesting to study the magnetism in  $SrMO_3$  in comparison with that of the perovskite and 2L hexagonal materials. This could also help to shed light on the striking differences of magnetic behavior in isostructural  $CSrNb_2$  and  $BaMO_3$ . In  $SrMO_3$ , a complex magnetic behavior is expected from the exchange topology, which results from the arrangement of pairs of face sharing  $MO_6$  linked connected by the octahedra corners. In this structure, direct Mn-Mn exchange interactions between  $Mn^{4+}$  ions in face sharing octahedra ( $J_D$ ) compete with the 90° AF-SE linkages through the face shared by  $MO_6$  octahedra ( $J_1$ ) as in  $BaMO_3$ , and 180° AF-SE linkages across the common oxygen of corner sharing  $MO_6$  octahedra ( $J_2$ ), like in  $CaMO_3$ . As in several hexagonal transition metal oxides or sulfides,  $J_D$  is probably very strong, since the metal-metal distance is much lower than that observed in the corresponding intermetallic compounds containing the same transition metal element<sup>13,14</sup>.

As first noticed by Battle et al.<sup>15</sup>,  $SrMO_3$  shows unusual magnetic properties: the magnetization data, which we have also measured (see Fig.2) show a transition above room temperature ( $T_S \approx 350K$ ), but neutron powder diffraction (NPD) demonstrates that this does not correspond to the AF ordering. AF order sets in only at lower temperatures, where zero field cooled and field cooled  $M(T)$  curves deviate ( $T_N = 278K$ )<sup>15</sup>. Recently, Ram an

spectroscopy was used to evidence a structural transformation in  $\text{SrMnO}_3$  below 200K<sup>16</sup>. To explain the subtle difference observed by Raman spectroscopy, the authors proposed a 4L to 6L transition, allowing the hexagonal symmetry to be retained.

In this article, we present a complete study of the magnetic and structural properties of  $\text{SrMnO}_3$ , using in combination electron microscopy, neutron powder diffraction (NPD) and high-resolution synchrotron X-ray powder diffraction (HR-SXPD).

## II. EXPERIMENTAL

Polycrystalline samples of  $\text{SrMnO}_3$  were synthesized by solid-state reaction in air of a stoichiometric mixture (1:0.5) of  $\text{SrCO}_3$  and  $\text{Mn}_2\text{O}_3$ . The powder was heated at 950 C during two weeks with intermediate grindings, then pelletized and sintered at 1000 C for 12 hrs. This low-temperature synthesis was determined from the phase diagrams<sup>10,11</sup> as the best route to obtain pure hexagonal 4L-structure without oxygen deficiency. Samples quality and stoichiometry were determined by preliminary neutron diffraction measurements.

At room temperature, the reconstruction of the reciprocal space was carried out with a JEOL 200 CX electron microscope and high resolution electron microscopy (HREM) images at room temperature were recorded using a TOPCON 002B microscope ( $C_s = 0.4 \text{ mm}$ ). The electron diffraction patterns versus temperature were collected with a JEOL 2010 electron microscope operating at 200kV and equipped with a double-tilt liquid N<sub>2</sub> sample holder (tilt 30°, 45°, and 90K < T 300K). All the patterns were recorded under the same experimental conditions, i.e. the same exposure time, the same electron beam alignment and the same beam intensity and increasing the temperature from 90K to 300K, in steps of 10 degrees, waiting for temperature stabilization before recording. The three microscopes are equipped with Energy Dispersive Analysis spectrometers (EDS), which allow determining the Sr/Mn ratio.

Magnetic susceptibility was collected under a magnetic field of 1000 Oe under zero-field cooled (ZFC) and field cooled (FC) processes. Data were collected on warming between 2K and 400K at a sweep rate of 1K/min, using a Vibrating Sample Magnetometer (Quantum Design, PPM S).

High resolution synchrotron and time-of-flight neutron powder diffraction data were collected at 100 and 350K, using the ID 31 beam line at the ESRF, Grenoble with a wavelength

$= 0.30001(2)\text{\AA}$ , and HRPD at the ISIS Facility (UK), respectively. Subsequent medium-resolution neutron diffraction data were collected on the General Materials (GEM) Diffractometer of the ISIS facility to study the temperature dependence of the crystal structure and the magnetic structure. Data sets at temperature between 1.9 and 300K with 25K steps were collected on warming using a standard He cryostat. The diffraction patterns were used to refine the  $\text{SrMnO}_3$  structure by the Rietveld method<sup>17</sup> using the FullProf suite (Ref.18). Symmetry analysis for the structural and magnetic phase transitions was performed using the BasIreps program, part of the FullProf suite as well as programs available on the Bilbao Crystallographic Server<sup>19</sup>.

### III. RESULTS

#### A. Magnetization measurements

The DC magnetic susceptibility of  $\text{SrMnO}_3$  between 2 and 400K is reported in Fig. 2. Plot of the inverse susceptibility, not shown, indicates that a Curie-Weiss behavior is not obeyed in this temperature range, in agreement with earlier results<sup>20</sup>. However, our results below 400K are qualitatively different to what was previously reported. Below 380K, there is a clear upturn in the susceptibility followed by a relatively shallow decrease below 300K. The upturn could be associated with the structural phase transition reported herein, and discussed in the following sections, as evidenced by X-ray and neutron diffraction. However, it was impossible to track precisely the structural details as a function of temperature due to the extremely weak intensities of the superlattice reflections and therefore confirm unambiguously the correlation between structural and magnetic behaviors. Also, this upturn could be associated to short-range magnetic correlations within the face-sharing  $\text{MnO}_6$  octahedra, as suggested by Battle et al.<sup>15</sup>.

At lower temperatures ( $T < 300\text{K}$ ) where  $\chi$  decreases, the behavior is clearly reminiscent of antiferromagnets. This is in agreement with previous work, in particular with the largely negative Weiss temperature of  $-1210\text{K}$  derived by susceptibility measurements at high temperature<sup>20</sup>. The determination of the Néel temperature from susceptibility alone is not straightforward due to the broad maximum observed in the variation of  $\chi$ . Battle and co-workers identified a Néel temperature of  $278\text{K}$  from Mossbauer spectroscopy on Fe-doped

samples<sup>15</sup>. Our measurements suggest the same Néel transition temperature since the susceptibility curves in field cooled (FC) and zero-field cooled (ZFC) conditions slightly deviates at around 280K. Moreover, this accident coincides with the onset of a long-range ordered antiferromagnetic structure evidenced by our neutron diffraction experiment, as discussed below.

## B. Crystal Structure

In this section, we report a detailed crystallographic characterization of  $\text{SrMnO}_3$  from electron microscopy and high-resolution X-ray and neutron powder diffraction experiments.

### 1. Transmission Electron Microscopy

A large number of crystallites have been analyzed by EDS and electron diffraction, confirming an homogeneous Sr/Mn ratio = 1 in the limit of the accuracy of the technique. The reconstruction of the reciprocal space was carried out by tilting the sample around the crystallographic axes. It evidences an hexagonal cell with  $a = 5.45\text{\AA}$  ( $a_p = 2a_p$  ( $a_p$  is the parameter of the ideal cubic perovskite cell)),  $c = 9.06\text{\AA}$  and the extinction condition  $hh2hl = 2n$ . These results are consistent with the 4L polytype proposed for  $\text{SrMnO}_3$  as well as the space group  $P6_3/mmc$  previously reported<sup>10,11</sup>. The [110] ED pattern at room temperature is given in Fig.3a. The quality of the crystallites was checked using HREM, in order to detect the presence of any intergrowth defects (variations in the layer stacking along  $c$ , i.e. the presence of different polytypes). The lattice images, not shown, confirm that the stacking of the 4L structure is quite perfect. The density of defects is very low (of the order a few events for a nanometer-sized crystallite), which is rather rare in the hexagonal polytypes, allowing one to conclude that these defects do not significantly affect the symmetry.

The reciprocal space was reconstructed at 90K, tilting especially around the  $c$  axis. One clearly observes two important points: first, the lattice parameters remain unchanged, especially  $c$ , attesting that the 4L stacking mode is retained and second, the appearance of another system of weak reflections,  $hh2hl = \text{no condition}$ , which clearly violate the mirror symmetry. This is illustrated comparing Fig.3a and 3b with the evolution of the [110] ED pattern between RT and 92K. At this step, a careful rotation around  $c$ , selecting the

[hk0] ED patterns with large h and k values, shows that, in our conditions of reflection, the Bragg peaks  $00l: l = 2n + 1$  are scarcely visible but not null. Increasing T, step by step, up to room temperature shows that the intensity of the extra reflections remain unchanged between 90K and 200K, it decreases from 200K to 265K and, lastly, disappears for  $T > 267K$  when keeping our working conditions constant. This transition temperature is probably an underestimate, due to the heating of the sample under electron beam irradiation.

## 2. Combined NPD and HR-SXPD refinements at $T = 350K$ and $T = 100K$

In agreement with the TEM results, high resolution X-ray and neutron powder diffraction indicate that a number of (hkl) Bragg reflections with odd l index appear at low temperature. In the synchrotron X-ray diffraction pattern at 100K, the strongest of these additional peaks is (221) whereas in the neutron data, two reflections indexed (221) and (223) in the hexagonal setting are the most clearly visible. The fact that these additional reflections appear at high value of the scattering vector ( $Q$ ) and are present in the X-ray data, indicate their nuclear origin. At 350K, the reflections are almost extinct but a close inspection of the diffraction pattern reveal a weak contribution even at this temperature. Nevertheless, their intensities at 350K are too weak to determine the change of structure. In this respect, the model of Battle et al., with hexagonal symmetry  $P6_3/mmc$ , remains a valid approximation at high temperature. The extracted parameters from the combined refinement of X-ray and neutron data at 350K, assuming  $P6_3/mmc$  symmetry, are reported in table I.

At low temperature, this model is obviously invalid due to the presence of new reflections. Also, our preliminary study with medium resolution neutron diffraction as a function of temperature, indicates that the thermal parameter of some atoms, in particular, O (1), increases when the temperature is lowered, suggesting that  $P6_3/mmc$  is a pseudo-symmetry. In agreement with our TEM results, NPD and HR-SXPD data are consistent with the absence of the c glide-plane symmetry operation. None of the maximal isotropy subgroups of order 2, as listed in the International Tables of crystallography<sup>21</sup>, is able to fit the data. The solution was found among isotropy subgroups of higher index, which are compatible with the Landau and Lifshitz conditions of the theory of second order phase transitions, as listed by Hatch and Stokes<sup>22</sup> or equivalently, by the program Isotropy<sup>23</sup>. The only solution fitting the data corresponds to the orthorhombic space group  $C22_1$  with a super-cell related to the

hexagonal cell in the following way:  $a_o = a_h$ ,  $b_o = a_h + 2b_h$ ,  $c_o = c_h$ . This phase transition is a perfect example of pseudo-symmetry problems since there are no direct indication of the orthorhombic symmetry from splitting of equivalent reflections or anisotropic broadening. The system remains metrically hexagonal within the very high resolution of our X-ray and neutron experiments; therefore in-plane lattice parameters were constrained accordingly in the refinements. This also indicates that the atomic displacements involved must be small enough to remain decoupled from the lattice strain.

In the low-temperature structure, the atomic positions for all atoms, with the exception of the Mn site, split into two orbits. In our model, all refinable atomic positions were allowed to vary, while thermal parameters of atoms belonging to the two related orbits were constrained to be equal. The combined X-ray and neutron Rietveld refinement, presented in Fig. 4, is in excellent agreement with the data. Reliability factors of the refinement and refined structural parameters are listed in Table I. It is important to note that the combined refinement is of crucial importance here because the difference in contrast in the X-ray and Neutron experiments (O is a strong neutron scatterer, Mn neutron scattering length is negative) is extremely selective.

The nature of the phase transition, involving all ions in the crystal, is difficult to comprehend without decomposing the respective atomic displacements. We have used group theory, to explain in details the symmetry descent across the phase transition. The atomic displacements, shown in Fig. 5, are decomposed in symmetry-adapted modes of the irreducible representation  $\Gamma_5$  corresponding to the observed symmetry descent. More details about the treatment with representation theory are given in Appendix A, and the basis vectors of these modes are reported in tables A. Figs. 5a and 5b represent individual modes while Fig. 5c shows the resulting displacements consistent with the final refinement of atomic positions. The transition involves a slight tilting of the corner-sharing  $Mn_2O_9$  units composed of 2 face-sharing  $MnO_6$  octahedra. This is coupled to a shear motion of  $Sr^{2+}$  cations in the ab-plane. It is clear that the largest displacements are associated with the O(1) ions which explain our preliminary results of large thermal displacements on this site in the hexagonal setting. The sequential refinements of GEM data ( $1.5K < T < 300K$ ) do not show any obvious discontinuity for most of the geometrical parameters of the structure: excepted for volume contraction, the Mn-O bond distances and angles within the  $Mn_2O_9$  units are temperature independent. The structural transition essentially manifests in the temperature



dependence of some of the Mn-O-Mn angles across corner sharing octahedra, which very slightly reduce by 2° in the low temperature phase. The Raman data<sup>16</sup> must therefore be reinterpreted in the light of the rather subtle transition we have established.

### C. Magnetic structure

Below room temperature, additional Bragg reflections are observed in the powder neutron diffraction patterns, which can all be indexed with a propagation vector  $k=0$  with respect to the C-centered orthorhombic crystallographic unit cell. These reflections are clearly magnetic in origin since their intensities decrease rapidly as a function of the scattering vector  $Q$ , following the magnetic form factor. We note that magnetic scattering and nuclear scattering attributable to the structural phase transition give rise to different contributions in the diffraction pattern, allowing to treat both problems separately. Symmetry analysis of the magnetic structure has been performed using representation analysis and is detailed in the appendix A. The magnetic representation decomposed into the direct sum of irreducible representations:

$$\Gamma_1 + \Gamma_2 + \Gamma_3 + \Gamma_4 \quad (1)$$

where all  $\Gamma_i$  ( $i=1,4$ ) are one-dimensional representations of the little group  $G_k$ , which in this case ( $k=0$ ) is simply the crystallographic space group. Only two modes,  $\Gamma_7$  or  $\Gamma_{10}$ , belonging to different representations  $\Gamma_3$  and  $\Gamma_4$ , fit the experimental data. These modes give the same arrangement of spins with components along the a- and b-directions respectively and are in fact equivalent due to the hexagonal pseudo-symmetry. In fact, these modes belong to a single irreducible representation when the analysis is performed in the hexagonal setting. For the same reason, it is impossible to determine the direction of the spins in the ab-plane, and we have arbitrarily chosen to direct them along the a-axis. The refinement, shown in Fig.6, is of very good quality. The global user-weighted  $\chi^2 = 1.30$ , and the Bragg R-Factors for each pattern are  $R_{Nuc} = 2.44\%$ ,  $R_{Nuc} = 2.29\%$ ,  $R_{Nuc} = 2.54\%$ ,  $R_{Mag} = 3.09\%$ ,  $R_{Mag} = 2.39\%$  and  $R_{Mag} = 7.58\%$  for the patterns collected on the 34:96, 63:62, and 91:30 detectors banks, respectively. The magnetic structure is reported in Fig.7. It can be described as a simple antiferromagnetic structure since the magnetic moments of all first neighbor Mn ions are aligned antiparallel.

The most surprising finding is the value of the manganese magnetic moment extracted

from our Rietveld refinements as a function of temperature, as shown in Fig.6. For a quenched orbital contribution, the expected ordered moment for high spin  $Mn^{4+}$  ions is  $3 \mu_B$  per Mn ion but the observed value, saturating at 2.27(1) at low temperature, is significantly reduced.

#### IV . D I S C U S S I O N

##### A . Structure

The nature of the structural phase transition and in particular its connection with the magnetic properties, are not immediately clear. The transition does not manifest as an abrupt decrease of the interatomic Mn-Mn distance, so that it cannot be obviously related to some magnetic exchange-striction, which could strengthen direct antiferromagnetic interactions over the superexchange interactions. In the measured temperature range, the Mn-Mn distance decreases smoothly ( $d_{Mn-Mn} = 2.485(2)$  at 100K and  $2.497(3)$  at 350K) following essentially the expected thermal expansion. Data collected on a finer temperature scale would be needed to exclude completely the presence of exchange striction in this material.

Even though it has not been precisely determined here, the structural phase transition temperature is certainly above 350K and it probably coincides with the changes observed in magnetization at  $T_s = 380K$ . Therefore, it has clearly no connection with the onset of magnetic order at  $T_N = 286K$ . In fact, preliminary neutron measurements show that the structural transition temperature increases when Ca is substituted for Sr in the system, highlighting the critical role of ionic radius on the A-site. From this, we conclude that the transition is primarily due to a steric effect. This probably influences indirectly the magnetic properties as follows. The distortion induces a small bending of the Mn-O-Mn angle between some corner sharing octahedra, which could reduce the electron transfer of the 3d electron between Mn pairs. This can accordingly enhance correlations associated to the direct exchange interactions inside each pair below  $T_s = 380K$ , before the magnetic ordering is established below  $T_N = 286K$ .

## B. Magnetism

Let's come back first to the exchange topology of  $\text{SrMnO}_3$ , as introduced in Fig.1. It is clear that for the superexchange path  $J_2$ , the nearly  $180^\circ$  Mn-O-Mn bond angle between corner-sharing  $\text{MnO}_6$  octahedra favors antiferromagnetic arrangement according to the Goodenough-Kanamori-Anderson (GKA) rules<sup>4,6</sup>. However, GKA rules predict a ferromagnetic superexchange interaction for the path  $J_1$  between Mn spins of face-sharing octahedra, since here, the Mn-O-Mn angle is nearly  $90^\circ$ . The observed antiferromagnetic arrangement between these Mn ions indicates that the exchange  $J_D$  through direct overlap of d orbitals, dominates over super-exchange interactions. The sign of the direct exchange interaction depends on the interatomic distance between Mn ions, with shorter bonds favoring an antiferromagnetic arrangement. The effect of interatomic distances has been systematically studied in Mn intermetallic compounds. In  $\text{R}(\text{Mn},\text{Fe})_6\text{A}$  (R: rare earth, A: Sn or Ge), a crossover from ferromagnetic to antiferromagnetic interactions was clearly observed for distances below  $2.61 \text{ \AA}$ <sup>13</sup>, whereas in various solid solutions derived from  $\text{MnSb}$ , that crossover is found for average Mn-Mn distances below  $2.83 \text{ \AA}$ <sup>14</sup>. A strong antiferromagnetic direct interaction arising from the small value of  $2.49 \text{ \AA}$  reported here for the Mn-Mn distance in  $\text{SrMnO}_3$  is perfectly consistent with the trend seen in intermetallic compounds.

Let us compare now the properties of the present pure, defect free and stoichiometric  $\text{SrMnO}_3$ , with that of  $\text{BaMnO}_3$  and  $\text{CaMnO}_3$  keeping in mind that most  $\text{CaMnO}_3$  compounds are oxygen deficient.  $\text{BaMnO}_3$ <sup>9</sup> and  $\text{CaMnO}_3$ <sup>24</sup> have also simple magnetic structures with AF arrangements of nearest neighbor Mn. The ordered moment reported for  $\text{BaMnO}_3$  and that extrapolated for stoichiometric  $\text{CaMnO}_3$ , fits the expected  $gS = 3 \mu_B$  value for high spin  $\text{Mn}^{4+}$  ions. This is not surprising considering  $\text{CaMnO}_3$  as a classical example of Heisenberg magnet with SE interactions. In the case of  $\text{BaMnO}_3$ , the magnetic ordering shows a very classical behavior, which probably results from the fact that the Mn-Mn distance is shorter ( $d_{\text{Mn-Mn}} = 2.40 \text{ \AA}$ ) than in  $\text{SrMnO}_3$ . The enhancement of direct antiferromagnetic exchange interaction in such case can explain why the moment saturates in  $\text{BaMnO}_3$  and not in  $\text{SrMnO}_3$ , despite the quasi-one dimensional effects expected from the infinite strings of face sharing octahedra in  $\text{BaMnO}_3$ .

From the presented data and the comparison with other materials, we therefore suggest that the Heisenberg/SE picture does not fully hold in  $\text{SrMnO}_3$ , and that this results from

an enhanced competition between SE and direct exchange interactions between neighboring Mn atoms in face sharing octahedra. Instead of isolated high spin  $Mn^{4+}$  ions, the proper magnetic unit should rather be considered as  $Mn_2O_9$  pairs. The loss of the  $Mn^{4+}$  ion identity is reminiscent to the loss of  $V^{3+}$  ion identity which has been discussed in the case of the prototype  $V_2O_3$  system<sup>25</sup>. Like  $SrMnO_3$ ,  $V_2O_3$  shows pairs of face sharing  $VO_6$  octahedra interconnected by the edges in the corundum structure. Here also, it has been concluded that the localized-electron unit in the antiferromagnetic insulating ground state may be the nearest-neighbor pairs, with the electrons delocalized within a pair, which has been later thoroughly confirmed by theoretical investigation of effective spin/orbital Hamiltonians<sup>26</sup>. The reduced moment in  $SrMnO_3$  at low temperatures indicates that something similar happens within the Mn-Mn dimers of  $SrMnO_3$ .

## V. CONCLUSION

In summary, we have shown that a structural transition does take place in  $SrMnO_3$ , but that this occurs at much higher temperature than previously reported from Raman scattering<sup>16</sup>, and is probably correlated with the transition observed in magnetization at 380K. The structural transformation does not correspond to a change of polytype, but to a subtle distortion within the 4L structure lowering the hexagonal  $P6_3/mmc$  symmetry to a  $C222_1$  orthorhombic pseudo-symmetry, which preserves the hexagonal metrics. This structural transition seems to be primarily due to steric effects, which only indirectly affects magnetic exchange. NPD reveals that  $SrMnO_3$  has a reduced moment at low temperatures. We interpret this might be due to the presence of delocalized electrons within  $Mn_2O_9$  pairs, a finding that deserves confirmation from theoretical studies of the electronic structure.

## APPENDIX A: SYMMETRY ANALYSIS OF THE STRUCTURAL AND MAGNETIC TRANSITIONS

The symmetry properties of the low temperature structure of  $SrMnO_3$  have been determined by representation analysis. The atomic positions are written

$$r_{ni} = r_i^0 + u_{ni} \quad (A1)$$

for atom  $s$  in crystallographic cells indexed by  $R_n$  that were at average positions  $r_i^0$  in the high temperature phase, which are now displaced by vectors  $u_{ni}$ . These displacement vectors are decomposed with the Fourier sum

$$u_{ni} = \sum_k u_k^i e^{2i \cdot k \cdot R_n} + u_k^i e^{2i \cdot k \cdot R_n} \quad (A 2)$$

where  $k$  is the wave vector characterizing how the translational symmetry is broken at the transition.

The symmetry relations between the vectors  $u_k^i$  for atom  $s$  of the same crystallographic orbit are obtained for each Irreducible Representation (Irrep) using the projection operator:

$$\hat{P} = \sum_{g \in G_k} D(g) g \quad (A 3)$$

The sum is over the symmetry elements  $g$  of the little group transforming  $k$  into an equivalent wave vector.  $D(g)$  are elements of the matrix representation of  $g$  for the Irrep. This operator projects an arbitrary set of displacement components on atom  $s$  of a crystallographic orbit of multiplicity  $L$  onto symmetrized basis functions (SBF). We conveniently write these SBF as  $\psi = \sum_{i=1:L} a_i e_i$ , where  $e_i$  represents the displacement vectors components on an atom  $i$  in the direction. An arbitrary set of linearly independent SBF are chosen from all the constructed ones. Working out with SBF belonging to single irreps is equivalent to assume a distortion compatible with a second order transition.

In our case, the propagation vector observed experimentally is  $k = (0,0,0)$ , a special case where the complex Fourier component  $u_k^i$  identifies with the real displacement  $u_{ni}$ . As always with  $k = (0,0,0)$ , all the symmetry elements of  $P6_3/mmc$  leave  $k$  invariant, hence,  $G_k$  coincides with the space group  $P6_3/mmc$ . Irreps and basis functions were obtained using the program BasIrreps. In our case however, the program outputs 8 real one-dimensional representations, and 4 two-dimensional complex representations. The SBF being expected to be real, it is desirable to transform the complex representations into real using an appropriate unitary similarity transformation matrix  $U$ , for which  $U^{-1} = (U)^T$  before projection. Using

$$U = \frac{1}{2} \begin{pmatrix} 1 & 0 & 1 & 0 \\ \frac{1}{\sqrt{3}} & \frac{1}{2} & \frac{1}{\sqrt{3}} & \frac{1}{2} \\ \frac{1}{\sqrt{3}} & -\frac{1}{2} & \frac{1}{\sqrt{3}} & -\frac{1}{2} \\ 1 & 1 & 1 & 1 \end{pmatrix} \quad (A 4)$$

real matrices  $d(g) = U^{-1} D(g) U$  for the Irreps  $\gamma_5, \gamma_6, \gamma_{11}, \gamma_{12}$  have been thus obtained from the complex matrices  $D(g)$ , which are output by BasIrreps (see tables II and III).

The projection of the SBF is illustrated for the two-dimensional representation labeled  $\Gamma_5$ , which correspond to the Irrep actually chosen at the phase transition in  $\text{SrMnO}_3$ . With the special choice of unitary transform, we could straightforwardly double check that the symmetry modes associated to the transition from  $P6_3/mmc$  to  $C222_1$  and given by the program SYMMODES of the Bilbao crystallographic server<sup>27</sup> indeed correspond to a subsets of the SBF calculated for the Irrep  $\Gamma_5$  by BasIreps.

Representation analysis is more general, and also applies to other type of phase transitions where atoms acquire a new scalar, vectorial, or tensorial property in the low-symmetry phase. Instead of dealing with atomic displacements (polar vectors) in the case of structural transitions, we can indeed deal with the appearance of a magnetic moment to treat the case of magnetic transitions:

$$n_i = S_k^i e^{2i \cdot k \cdot R_n} + S_k^i e^{2i \cdot k \cdot R_n} \quad (\text{A } 5)$$

The only change in the orthogonalization procedure and the construction of the SBF summing this time the symmetry relation of the Fourier components  $S_k^i$ , is the action of the space group operation  $g$  in Eq A 3, which is different for axial and polar vectors. We similarly obtained the symmetry analysis of the possible magnetic structure of  $\text{SrMnO}_3$ , which is summarized in table V.

- 
- <sup>1</sup> E. Dagotto, T. Hotta, and A. Moreo, Phys. Rep. 344, 1 (2001).
  - <sup>2</sup> J. Orenstein and A. Millis, Science 288, 468 (2000).
  - <sup>3</sup> A. Imada, M. Fujimori and T. Y., Rev. Mod. Phys. 70, 1039 (1998).
  - <sup>4</sup> J. B. Goodenough, Phys. Rev. 100, 564 (1955).
  - <sup>5</sup> P. Anderson, Phys. Rev. 115, 2 (1959).
  - <sup>6</sup> J. Kanamori, J. Phys. Chem. Solids 10, 87 (1959).
  - <sup>7</sup> T. E. Mason, B. D. Gaulin, and M. F. Collins, Phys. Rev. B 39(1), 586 (1989).
  - <sup>8</sup> A. Harrison, M. F. Collins, J. Abu-Daayeh, and C. V. Stager, Phys. Rev. B 43(1), 679 (1991).
  - <sup>9</sup> A. N. Christensen and G.OLLIVIER, J. Solid State Chem. 4, 131 (1972).
  - <sup>10</sup> T. Negas and R. S. Roth, J. Solid State Chem. 1, 409 (1970).
  - <sup>11</sup> Y. Syono, S. Akimoto, and K. Kohn, J. Phys. Soc. Jpn. 26, 993 (1969).
  - <sup>12</sup> O. Chmaissem, Phys. Rev. B 64, 134412 (2001).

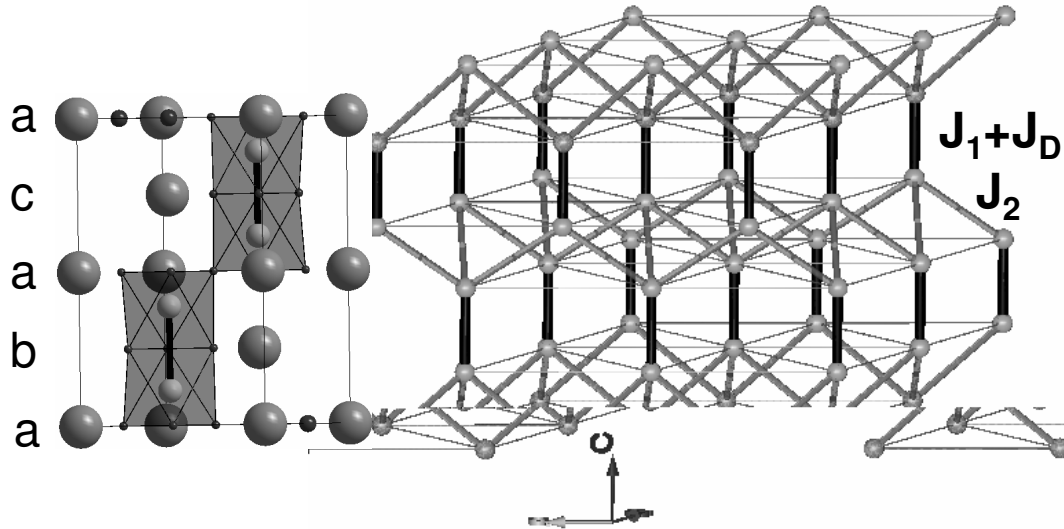


FIG. 1: Left panel: Crystal structure of  $\text{SrMnO}_3$  viewed along the  $[110]$  direction. The Sr, Mn and O atoms are shown as large grey spheres, small grey spheres and black spheres respectively. Face-sharing  $\text{MnO}_6$  octahedra are also represented as transparent grey units; Right panel: magnetic exchange topology of the Mn sublattice. Black bonds represent magnetic exchange between Mn ions of the  $\text{Mn}_2\text{O}_9$  units, composed of antiferromagnetic direct exchange ( $J_D$ ) and ferromagnetic super-exchange ( $J_1$ ). Grey bonds represent super-exchange interactions ( $J_2$ ) between Mn ions of the hexagonal units. See text for details.

<sup>13</sup> G. Marasinghe, J. Han, W. James, W. Yelon, and N. Ali, J. Appl. Phys. 91, 7863 (2002).

<sup>14</sup> V. Bai and T. Rajasekharan, J. of Mag. Mag. Mat. 42, 198 (1984).

<sup>15</sup> P. Battle, T. Gibb, and C. Jones, J. Solid State Chem. 74, 60 (1988).

<sup>16</sup> A. Sacchetti, M. Baldini, F. Crispoldi, P. Postorino, P. Dore, A. Nucara, C. Martin, and A. Maignan, Phys. Rev. B 72 (17), 172407 (2005).

<sup>17</sup> H. Rietveld, J. Appl. Cryst. 2, 65 (1969).

<sup>18</sup> J. Rodriguez-Carvajal, Physica B 192, 55 (1993).

<sup>19</sup> M. I. Arroyo, J. M. Perez-Mato, C. Capillas, E. Kroumova, S. Ivantchev, G. Madariaga, A. Kirov, and H. Wondratschek, Z. Kristallogr. 221 (1), 15 (2006).

<sup>20</sup> B. L. Chamberland, A. W. Sleight, and J. F. Weiher, J. Solid State Chem. 1, 506 (1970).

<sup>21</sup> T. Hahn, ed., International Tables for Crystallography, Volume A: Space Group Symmetry (IUCr, D. Reidel Publishing Company, 1983).

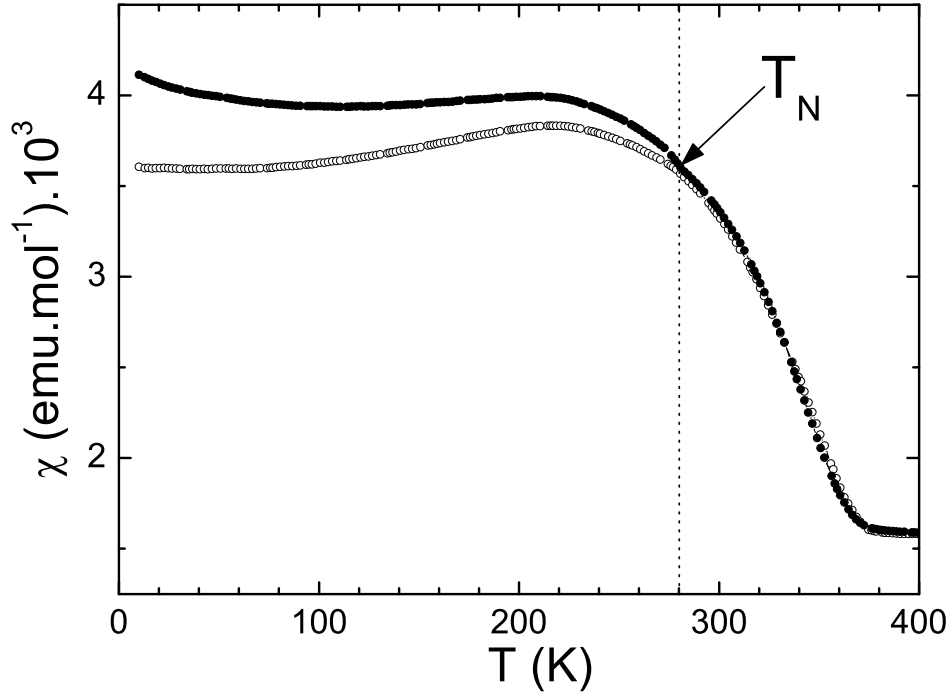


FIG. 2: DC Magnetic susceptibility of  $\text{SrMnO}_3$  under a magnetic field of 1000 Oe. Data in zero-field cooled (grey symbols) and field cooled (black) conditions are shown.

<sup>22</sup> H. T. Stokes and D. M. Hatch, Phys. Rev. B 30 (9), 4962 (1984).

<sup>23</sup> H. T. Stokes and D. M. Hatch, ISOTROPY (2002), <http://stokes.byu.edu/isotropy.html>.

<sup>24</sup> E. O. Wollan et al., Phys. Rev. 100, 545 (1955).

<sup>25</sup> J. W. Allen, Phys. Rev. Lett. 36 (21), 1249 (1976).

<sup>26</sup> S. Dimatteo, N. B. Perkins, and C. R. Natoli, Phys. Rev. B 65 (5), 054413 (2002).

<sup>27</sup> C. Capillas, E. Kroumova, M. I. Aroyo, J. M. Perez-Mato, H. T. Stokes, and D. M. Hatch, J. Appl. Crystallogr. 36 (3 Part 2), 953 (2003).



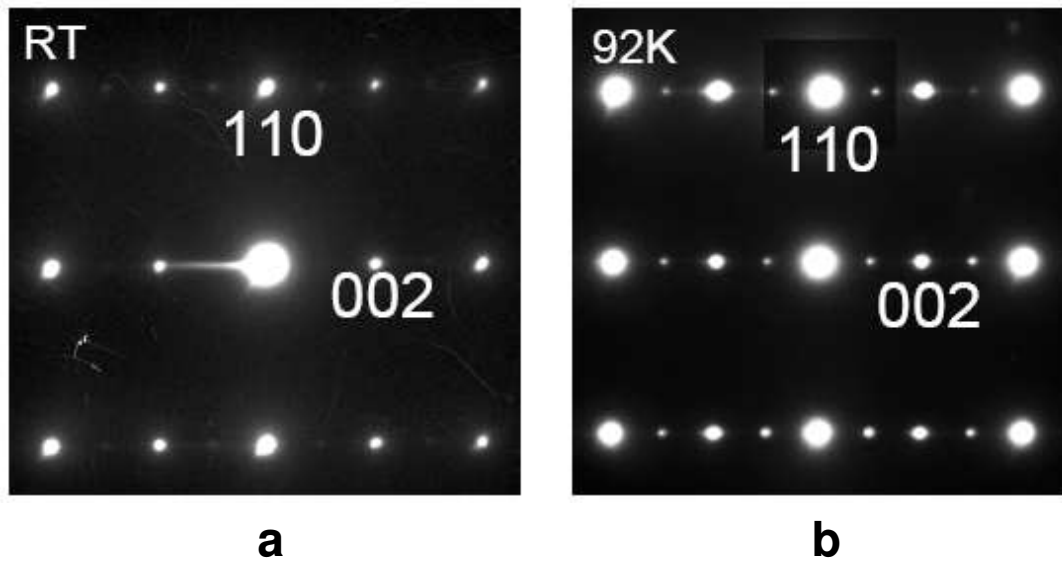


FIG. 3:  $[110]$  ED pattern of  $\text{SrMnO}_3$  at RT (a) and 92K (b). The low temperature data shows the appearance of another system of weak reflections,  $h\frac{1}{2}h11=$  no condition, which clearly violate the mirror c. A careful rotation around  $c$ , selecting the  $[hk0]$  ED patterns with large  $h$  and  $k$  values, shows that, in our conditions of reflection, the conditions  $00l: l=2n+1$  are scarcely visible but not null and hence, are not due to double diffraction.

T = 350K : P 6 <sub>3</sub> =n m m c, a <sub>h</sub> = b <sub>h</sub> = 5.461 (1)Å, c = 9.093 (2)Å <sup>a</sup>					
	Sr <sub>1</sub> (2a)	Sr <sub>2</sub> (4f)	Mn (4f)	O <sub>1</sub> (6g)	O <sub>2</sub> (6h)
Position	(0,0,0)	(1/3,2/3,1/4)	(1/3,2/3,z)	(1/2,0,0)	(-x,x,3/4)
			z= 0.61264 ( 20)		x= 0.81858 ( 25)
B <sub>iso</sub>	0.67 ( 8)	0.40 (8)	0.26 (7)	0.69 (8)	0.40 (7)
T = 100K : C 222 <sub>1</sub> , a = 5.4435 (1)Å, b <sup>P</sup> <sub>3b<sub>h</sub></sub> = 9.4211 (2)Å, c = 9.0630 (1)Å <sup>b</sup>					
Atom	Wyck	x	y	z	B <sub>iso</sub>
Sr1	4a	0.0096 (8)	0	0	0.44 (3)
Sr2	4b	0	1/3	1/4	0.44 (3)
Mn	8c	-0.0123 (8)	1/3	0.6131 (2)	0.33 (4)
O 11	4a	0.5212 (6)	0	0	0.64 (4)
O 12	8c	0.7712 (6)	1/4	0.0085 (5)	0.64 (4)
O 21	4b	0	-0.1798 (2)	1/4	0.52 (4)
O 22	8c	0.2696 (3)	0.0899 (1)	0.2412 (6)	0.52 (4)

<sup>a</sup>NPD  $\chi^2 = 8.47$  R<sub>Bragg</sub> = 5.23% ; HR-SXPD  $\chi^2 = 6.91$  R<sub>Bragg</sub> = 5.71%

<sup>b</sup>NPD  $\chi^2 = 4.37$  R<sub>Bragg</sub> = 2.64% ; HR-SXPD  $\chi^2 = 2.51$  R<sub>Bragg</sub> = 3.78%

TABLE I: Structural parameters of SrMnO<sub>3</sub>, obtained by combined refinements of HRPD-ISIS, and ID 31-ESRF neutron and synchrotron data. At 100K, structural parameters have been constrained as: y (Sr<sub>2</sub>) = 1/3, y (Mn) = 1/3, y (O<sub>12</sub>) = 1/4, x (O<sub>22</sub>) = -3/2y (O<sub>21</sub>) and x (O<sub>22</sub>) = -1/2y (O<sub>21</sub>). We also constrained the isotropic temperature factors to be the same for each chemical species.

Ireps		Symmetry operators					
IT symbol	1	3+ 0,0,z	2 (0,0,1/2) 0,0,z	2 x,x,0	3- 0,0,z	6- (0,0,1/2) 0,0,z	
	x;y;z	x; y;z + 1=2	y;x y;z	y; x + y;z + 1=2	x + y; x;z	x y;x;z + 1=2	
IT symbol	2 0,y,0	2 x,-x,1/4	6+ (0,0,1/2) 0,0,z	2 x,0,0	2 2x,x,1/4	2 x,2x,1/4	
	y;x; z	y; x; z 1=2	x y; y; z	x + y;y; z 1=2	x; x + y; z	x;x y; z 1=2	
IT symbol	-1 0,0,0	-3+ 0,0,z; 0,0,0	m x,y,1/4	m x,-x,z	-3- 0,0,z; 0,0,0	-6- 0,0,z; 0,0,1/4	
	x; y; z	x;y; z 1=2	y; x + y; z	y;x y; z 1=2	x y;x; z	x + y; x; z 1=2	
IT symbol	m 2x,x,2z	c x,x,z	-6+ 0,0,z; 0,0,1/4	m x,2x,z	c 0,y,z	c x,0,z	
	y; x;z	y;x;z + 1=2	x + y;y;z	x y; y;z + 1=2	x;x y;z	x; x + y;z + 1=2	
1	1	1	1	1	1	1	
	1	1	1	1	1	1	
	1	1	1	1	1	1	
	1	1	1	1	1	1	
2	1	1	1	1	1	1	
	1	1	1	1	1	1	
	-1	-1	-1	-1	-1	-1	
	-1	-1	-1	-1	-1	-1	
3	1	1	1	1	1	1	
	-1	-1	-1	-1	-1	-1	
	1	1	1	1	1	1	
	-1	-1	-1	-1	-1	-1	
4	1	1	1	1	1	1	
	-1	-1	-1	-1	-1	-1	
	-1	-1	-1	-1	-1	-1	
	1	1	1	1	1	1	
5	1 0	1 0	$\frac{1}{2} \frac{p-3}{2}$	$\frac{1}{2} \frac{p-3}{2}$	$\frac{1}{2} \frac{p-3}{2}$	$\frac{1}{2} \frac{p-3}{2}$	
	0 1	0 1	$\frac{p-3}{2} \frac{1}{4}$	$\frac{p-3}{2} \frac{1}{4}$	$\frac{p-3}{2} \frac{1}{2}$	$\frac{p-3}{2} \frac{1}{2}$	
	$\frac{1}{2} \frac{p-3}{2}$	$\frac{1}{2} \frac{p-3}{2}$	1 0	1 0	$\frac{1}{2} \frac{p-3}{2}$	$\frac{1}{2} \frac{p-3}{2}$	
	$\frac{p-3}{2} \frac{1}{2}$	$\frac{p-3}{2} \frac{1}{2}$	0 1	0 1	$\frac{1}{2} \frac{p-3}{2}$	$\frac{1}{2} \frac{p-3}{2}$	
	1 0	1 0	$\frac{1}{2} \frac{p-3}{2}$	$\frac{1}{2} \frac{p-3}{2}$	$\frac{1}{2} \frac{p-3}{2}$	$\frac{1}{2} \frac{p-3}{2}$	
	0 1	0 1	$\frac{p-3}{2} \frac{1}{2}$	$\frac{p-3}{2} \frac{1}{2}$	$\frac{1}{2} \frac{p-3}{2}$	$\frac{1}{2} \frac{p-3}{2}$	
	$\frac{1}{2} \frac{p-3}{2}$	$\frac{1}{2} \frac{p-3}{2}$	1 0	1 0	$\frac{1}{2} \frac{p-3}{2}$	$\frac{1}{2} \frac{p-3}{2}$	
	$\frac{p-3}{2} \frac{1}{4}$	$\frac{p-3}{2} \frac{1}{4}$	0 1	0 1	$\frac{1}{2} \frac{p-3}{2}$	$\frac{1}{2} \frac{p-3}{2}$	
	1 0	1 0	$\frac{1}{2} \frac{p-3}{2}$	$\frac{1}{2} \frac{p-3}{2}$	$\frac{1}{2} \frac{p-3}{2}$	$\frac{1}{2} \frac{p-3}{2}$	
	0 1	0 1	$\frac{p-3}{2} \frac{1}{2}$	$\frac{p-3}{2} \frac{1}{2}$	$\frac{1}{2} \frac{p-3}{2}$	$\frac{1}{2} \frac{p-3}{2}$	
	$\frac{1}{2} \frac{p-3}{2}$	$\frac{1}{2} \frac{p-3}{2}$	1 0	1 0	$\frac{1}{2} \frac{p-3}{2}$	$\frac{1}{2} \frac{p-3}{2}$	
	$\frac{p-3}{2} \frac{1}{2}$	$\frac{p-3}{2} \frac{1}{2}$	0 1	0 1	$\frac{1}{2} \frac{p-3}{2}$	$\frac{1}{2} \frac{p-3}{2}$	
6	1 0	1 0	$\frac{1}{2} \frac{p-3}{2}$	$\frac{1}{2} \frac{p-3}{2}$	$\frac{1}{2} \frac{p-3}{2}$	$\frac{1}{2} \frac{p-3}{2}$	
	0 1	0 1	$\frac{p-3}{2} \frac{1}{4}$	$\frac{p-3}{2} \frac{1}{4}$	$\frac{p-3}{2} \frac{1}{2}$	$\frac{p-3}{2} \frac{1}{2}$	
	$\frac{1}{2} \frac{p-3}{2}$	$\frac{1}{2} \frac{p-3}{2}$	1 0	1 0	$\frac{1}{2} \frac{p-3}{2}$	$\frac{1}{2} \frac{p-3}{2}$	
	$\frac{p-3}{2} \frac{1}{4}$	$\frac{p-3}{2} \frac{1}{4}$	0 1	0 1	$\frac{1}{2} \frac{p-3}{2}$	$\frac{1}{2} \frac{p-3}{2}$	
	1 0	1 0	$\frac{1}{2} \frac{p-3}{2}$	$\frac{1}{2} \frac{p-3}{2}$	$\frac{1}{2} \frac{p-3}{2}$	$\frac{1}{2} \frac{p-3}{2}$	
	0 1	0 1	$\frac{p-3}{2} \frac{1}{2}$	$\frac{p-3}{2} \frac{1}{2}$	$\frac{1}{2} \frac{p-3}{2}$	$\frac{1}{2} \frac{p-3}{2}$	
	$\frac{1}{2} \frac{p-3}{2}$	$\frac{1}{2} \frac{p-3}{2}$	1 0	1 0	$\frac{1}{2} \frac{p-3}{2}$	$\frac{1}{2} \frac{p-3}{2}$	
	$\frac{p-3}{2} \frac{1}{2}$	$\frac{p-3}{2} \frac{1}{2}$	0 1	0 1	$\frac{1}{2} \frac{p-3}{2}$	$\frac{1}{2} \frac{p-3}{2}$	
	1 0	1 0	$\frac{1}{2} \frac{p-3}{2}$	$\frac{1}{2} \frac{p-3}{2}$	$\frac{1}{2} \frac{p-3}{2}$	$\frac{1}{2} \frac{p-3}{2}$	
	0 1	0 1	$\frac{p-3}{2} \frac{1}{2}$	$\frac{p-3}{2} \frac{1}{2}$	$\frac{1}{2} \frac{p-3}{2}$	$\frac{1}{2} \frac{p-3}{2}$	
	$\frac{1}{2} \frac{p-3}{2}$	$\frac{1}{2} \frac{p-3}{2}$	1 0	1 0	$\frac{1}{2} \frac{p-3}{2}$	$\frac{1}{2} \frac{p-3}{2}$	
	$\frac{p-3}{2} \frac{1}{2}$	$\frac{p-3}{2} \frac{1}{2}$	0 1	0 1	$\frac{1}{2} \frac{p-3}{2}$	$\frac{1}{2} \frac{p-3}{2}$	

TABLE II: Representative matrices  $d_i(g)$  for each irreducible representation  $\Gamma_i$  of the elements  $g$  belonging to the group of the wave vector  $G_k = P6_3/mmc$  for the space group  $G = P6_3/mmc$  and  $k = (0\ 0\ 0)$

Ireps		Symmetry operators					
IT symbol	1	3+ 0,0,z	2 (0,0,1/2) 0,0,z	2 x,x,0	3- 0,0,z	6- (0,0,1/2) 0,0,z	
	x;y;z	x; y;z + 1=2	y;x y;z	y; x + y;z + 1=2	x + y; x;z	x y;x;z + 1=2	
IT symbol	2 0,y,0	2 x,-x,1/4	6+ (0,0,1/2) 0,0,z	2 x,0,0	2 2x,x,1/4	2 x,2x,1/4	
	y;x; z	y; x; z 1=2	x y; y; z	x + y;y; z 1=2	x; x + y; z	x;x y; z 1=2	
IT symbol	-1 0,0,0	-3+ 0,0,z; 0,0,0	m x,y,1/4	m x,-x,z	-3- 0,0,z; 0,0,0	-6- 0,0,z; 0,0,1/4	
	x; y; z	x;y; z 1=2	y; x + y; z	y;x y; z 1=2	x y;x; z	x + y; x; z 1=2	
IT symbol	m 2x,x,2z	c x,x,z	-6+ 0,0,z; 0,0,1/4	m x,2x,z	c 0,y,z	c x,0,z	
	y; x;z	y;x;z + 1=2	x + y;y;z	x y; y;z + 1=2	x;x y;z	x; x + y;z + 1=2	
7	1	-1	1	-1	1	-1	
	1	-1	1	-1	1	-1	
	1	-1	1	-1	1	-1	
	1	-1	1	-1	1	-1	
8	1	-1	1	-1	1	-1	
	1	-1	1	-1	1	-1	
	-1	1	-1	1	-1	1	
	-1	1	-1	1	-1	1	
9	1	-1	1	-1	1	-1	
	-1	1	-1	1	-1	1	
	1	-1	1	-1	1	-1	
	-1	1	-1	1	-1	1	
10	1	-1	1	-1	1	-1	
	-1	1	-1	1	-1	1	
	-1	1	-1	1	-1	1	
	1	-1	1	-1	1	-1	
11	1 !	-1 !	1 !	-1 !	1 !	-1 !	
	1 0	1 0	$\frac{1}{2} \frac{\sqrt{3}}{2}$	$\frac{1}{2} \frac{\sqrt{3}}{2}$	$\frac{1}{2} \frac{\sqrt{3}}{2}$	$\frac{1}{2} \frac{\sqrt{3}}{2}$	
	0 1	0 1	$\frac{\sqrt{3}}{2} \frac{1}{4}$	$\frac{\sqrt{3}}{2} \frac{1}{2}$	$\frac{\sqrt{3}}{2} \frac{1}{2}$	$\frac{\sqrt{3}}{2} \frac{1}{2}$	
	$\frac{1}{2} \frac{\sqrt{3}}{2}$	$\frac{1}{2} \frac{\sqrt{3}}{2}$	1 0	1 0	$\frac{1}{2} \frac{\sqrt{3}}{2}$	$\frac{1}{2} \frac{\sqrt{3}}{2}$	
	$\frac{\sqrt{3}}{2} \frac{1}{2}$	$\frac{\sqrt{3}}{2} \frac{1}{4}$	0 1	0 1	$\frac{\sqrt{3}}{2} \frac{1}{2}$	$\frac{\sqrt{3}}{2} \frac{1}{2}$	
	1 0	1 0	$\frac{1}{2} \frac{\sqrt{3}}{2}$	$\frac{1}{2} \frac{\sqrt{3}}{2}$	$\frac{1}{2} \frac{\sqrt{3}}{2}$	$\frac{1}{2} \frac{\sqrt{3}}{2}$	
	0 1	0 1	$\frac{\sqrt{3}}{2} \frac{1}{2}$	$\frac{\sqrt{3}}{2} \frac{1}{4}$	$\frac{\sqrt{3}}{2} \frac{1}{2}$	$\frac{\sqrt{3}}{2} \frac{1}{2}$	
	$\frac{1}{2} \frac{\sqrt{3}}{2}$	$\frac{1}{2} \frac{\sqrt{3}}{2}$	1 0	1 0	$\frac{1}{2} \frac{\sqrt{3}}{2}$	$\frac{1}{2} \frac{\sqrt{3}}{2}$	
	$\frac{\sqrt{3}}{2} \frac{1}{4}$	$\frac{\sqrt{3}}{2} \frac{1}{2}$	0 1	0 1	$\frac{\sqrt{3}}{2} \frac{1}{2}$	$\frac{\sqrt{3}}{2} \frac{1}{2}$	
	1 0	1 0	$\frac{1}{2} \frac{\sqrt{3}}{2}$	$\frac{1}{2} \frac{\sqrt{3}}{2}$	$\frac{1}{2} \frac{\sqrt{3}}{2}$	$\frac{1}{2} \frac{\sqrt{3}}{2}$	
	0 1	0 1	$\frac{\sqrt{3}}{2} \frac{1}{4}$	$\frac{\sqrt{3}}{2} \frac{1}{2}$	$\frac{\sqrt{3}}{2} \frac{1}{2}$	$\frac{\sqrt{3}}{2} \frac{1}{2}$	
	$\frac{1}{2} \frac{\sqrt{3}}{2}$	$\frac{1}{2} \frac{\sqrt{3}}{2}$	1 0	1 0	$\frac{1}{2} \frac{\sqrt{3}}{2}$	$\frac{1}{2} \frac{\sqrt{3}}{2}$	
12	1 !	-1 !	1 !	-1 !	1 !	-1 !	
	1 0	1 0	$\frac{1}{2} \frac{\sqrt{3}}{2}$	$\frac{1}{2} \frac{\sqrt{3}}{2}$	$\frac{1}{2} \frac{\sqrt{3}}{2}$	$\frac{1}{2} \frac{\sqrt{3}}{2}$	
	0 1	0 1	$\frac{\sqrt{3}}{2} \frac{1}{4}$	$\frac{\sqrt{3}}{2} \frac{1}{2}$	$\frac{\sqrt{3}}{2} \frac{1}{2}$	$\frac{\sqrt{3}}{2} \frac{1}{2}$	
	$\frac{1}{2} \frac{\sqrt{3}}{2}$	$\frac{1}{2} \frac{\sqrt{3}}{2}$	1 0	1 0	$\frac{1}{2} \frac{\sqrt{3}}{2}$	$\frac{1}{2} \frac{\sqrt{3}}{2}$	
	$\frac{\sqrt{3}}{2} \frac{1}{4}$	$\frac{\sqrt{3}}{2} \frac{1}{2}$	0 1	0 1	$\frac{\sqrt{3}}{2} \frac{1}{2}$	$\frac{\sqrt{3}}{2} \frac{1}{2}$	
	1 0	1 0	$\frac{1}{2} \frac{\sqrt{3}}{2}$	$\frac{1}{2} \frac{\sqrt{3}}{2}$	$\frac{1}{2} \frac{\sqrt{3}}{2}$	$\frac{1}{2} \frac{\sqrt{3}}{2}$	
	0 1	0 1	$\frac{\sqrt{3}}{2} \frac{1}{2}$	$\frac{\sqrt{3}}{2} \frac{1}{4}$	$\frac{\sqrt{3}}{2} \frac{1}{2}$	$\frac{\sqrt{3}}{2} \frac{1}{2}$	
	$\frac{1}{2} \frac{\sqrt{3}}{2}$	$\frac{1}{2} \frac{\sqrt{3}}{2}$	1 0	1 0	$\frac{1}{2} \frac{\sqrt{3}}{2}$	$\frac{1}{2} \frac{\sqrt{3}}{2}$	
	$\frac{\sqrt{3}}{2} \frac{1}{2}$	$\frac{\sqrt{3}}{2} \frac{1}{4}$	0 1	0 1	$\frac{\sqrt{3}}{2} \frac{1}{2}$	$\frac{\sqrt{3}}{2} \frac{1}{2}$	
	1 0	1 0	$\frac{1}{2} \frac{\sqrt{3}}{2}$	$\frac{1}{2} \frac{\sqrt{3}}{2}$	$\frac{1}{2} \frac{\sqrt{3}}{2}$	$\frac{1}{2} \frac{\sqrt{3}}{2}$	
	0 1	0 1	$\frac{\sqrt{3}}{2} \frac{1}{4}$	$\frac{\sqrt{3}}{2} \frac{1}{2}$	$\frac{\sqrt{3}}{2} \frac{1}{2}$	$\frac{\sqrt{3}}{2} \frac{1}{2}$	
	$\frac{1}{2} \frac{\sqrt{3}}{2}$	$\frac{1}{2} \frac{\sqrt{3}}{2}$	1 0	1 0	$\frac{1}{2} \frac{\sqrt{3}}{2}$	$\frac{1}{2} \frac{\sqrt{3}}{2}$	

TABLE III: Continuation of Table II

Atom : Sr1 <sub>1</sub> at position (0;0;0)						
SYMM	x,y,z	-x,-y,z+ 1/2				
Atom s:	Sr1 <sub>1</sub>	Sr1 <sub>2</sub>				
1	( 1 0 0)	( -1 0 0)				
2	( -1 -2 0)	( 1 2 0)				
Atom : Mn <sub>1</sub> at position ( $\frac{1}{3}$ $\frac{2}{3}$ 0;6129)						
SYMM	x,y,z	-x,-y,z+ 1/2	y,x,-z	-y,-x,-z+ 1/2		
Atom s:	Mn <sub>1</sub>	Mn <sub>2</sub>	Mn <sub>3</sub>	Mn <sub>4</sub>		
3	( 1 0 0)	( -1 0 0)	( 1 0 0)	( -1 0 0)		
4	( -1 -2 0)	( 1 2 0)	( -1 -2 0)	( 1 2 0)		
Atom : O1 <sub>1</sub> at position ( $\frac{1}{2}$ 0 0)						
SYMM	x,y,z	-x,-y,z+ 1/2	-y,x-y,z	y,-x+ y,z+ 1/2	-x+ y,-x,z	x-y,x,z+ 1/2
Atom s:	O1 <sub>1</sub>	O1 <sub>2</sub>	O1 <sub>3</sub>	O1 <sub>4</sub>	O1 <sub>5</sub>	O1 <sub>6</sub>
5	( 2 0 0)	( -2 0 0)	( 0 -1 0)	( 0 1 0)	( 1 1 0)	( -1 -1 0)
6	( 0 0 0)	( 0 0 0)	( -2 -1 0)	( 2 1 0)	( -1 1 0)	( 1 -1 0)
7	( 0 0 0)	( 0 0 0)	( 0 0 1)	( 0 0 1)	( 0 0 -1)	( 0 0 -1)
8	( 0 0 0)	( 0 0 0)	( 0 -1 0)	( 0 1 0)	( -1 -1 0)	( 1 1 0)
9	( 0 0 0)	( 0 0 0)	( 0 1 0)	( 0 -1 0)	( 1 1 0)	( -1 -1 0)
10	( 0 0 2)	( 0 0 2)	( 0 0 -1)	( 0 0 -1)	( 0 0 -1)	( 0 0 -1)
Atom O2 <sub>1</sub> at position ( 0.8209 0.8209 $\frac{3}{4}$ )						
SYMM	x,y,z	-x,-y,z+ 1/2	-y,x-y,z	y,-x+ y,z+ 1/2	-x+ y,-x,z	x-y,x,z+ 1/2
Atom s:	O2 <sub>1</sub>	O2 <sub>2</sub>	O2 <sub>3</sub>	O2 <sub>4</sub>	O2 <sub>5</sub>	O2 <sub>6</sub>
11	( 0 0 1)	( 0 0 1)	( 0 0 0)	( 0 0 0)	( 0 0 -1)	( 0 0 -1)
12	( 0 0 1)	( 0 0 1)	( 0 0 -2)	( 0 0 -2)	( 0 0 1)	( 0 0 1)

TABLE IV :Basis functions  $\chi_i$  of representation  $\chi_5$ , for each crystallographic site of SrMnO<sub>3</sub>.

Irreps					
IT symbol	1	2	(0,0,1/2) 0,0,z	2 0,y,1/4	2 x,0,0
G <sub>k</sub>	x;y;z	x; y;z + 1=2	x;y; z + 1=2	x; y; z	
1	1	1	1	1	
2	1	1	-1	-1	
3	1	-1	1	-1	
4	1	-1	-1	1	
SBF					
Atom s	M n <sub>1</sub>	M n <sub>2</sub>	M n <sub>3</sub>	M n <sub>4</sub>	
Position	x;y;z	x; y;z + 1=2	x;y; z + 1=2	x; y; z	
1	(1 0 0)	( 1 0 0)	( 1 0 0)	(1 0 0)	
2	(0 1 0)	(0 1 0)	(0 1 0)	(0 1 0)	
3	(0 0 1)	(0 0 1)	(0 0 1)	(0 0 1)	
3	(1 0 0)	( 1 0 0)	(1 0 0)	( 1 0 0)	
4	(0 1 0)	(0 1 0)	(0 1 0)	(0 1 0)	
5	(0 0 1)	(0 0 1)	(0 0 1)	(0 0 1)	
6	(1 0 0)	(1 0 0)	( 1 0 0)	( 1 0 0)	
7	(0 1 0)	(0 1 0)	(0 1 0)	(0 1 0)	
8	(0 0 1)	(0 0 1)	(0 0 1)	(0 0 1)	
9	(1 0 0)	(1 0 0)	(1 0 0)	(1 0 0)	
10	(0 1 0)	(0 1 0)	(0 1 0)	(0 1 0)	
11	(0 0 1)	(0 0 1)	(0 0 1)	(0 0 1)	

TABLE V : IRREPS for the little group  $G_k = G$  of  $G = C 222_1$  and  $k = (0;0;0)$  and SBF for the orbit of the starting atom  $M n_1$  at position the  $(-0.0120 \ 0.3333 \ 0.6130)$ .

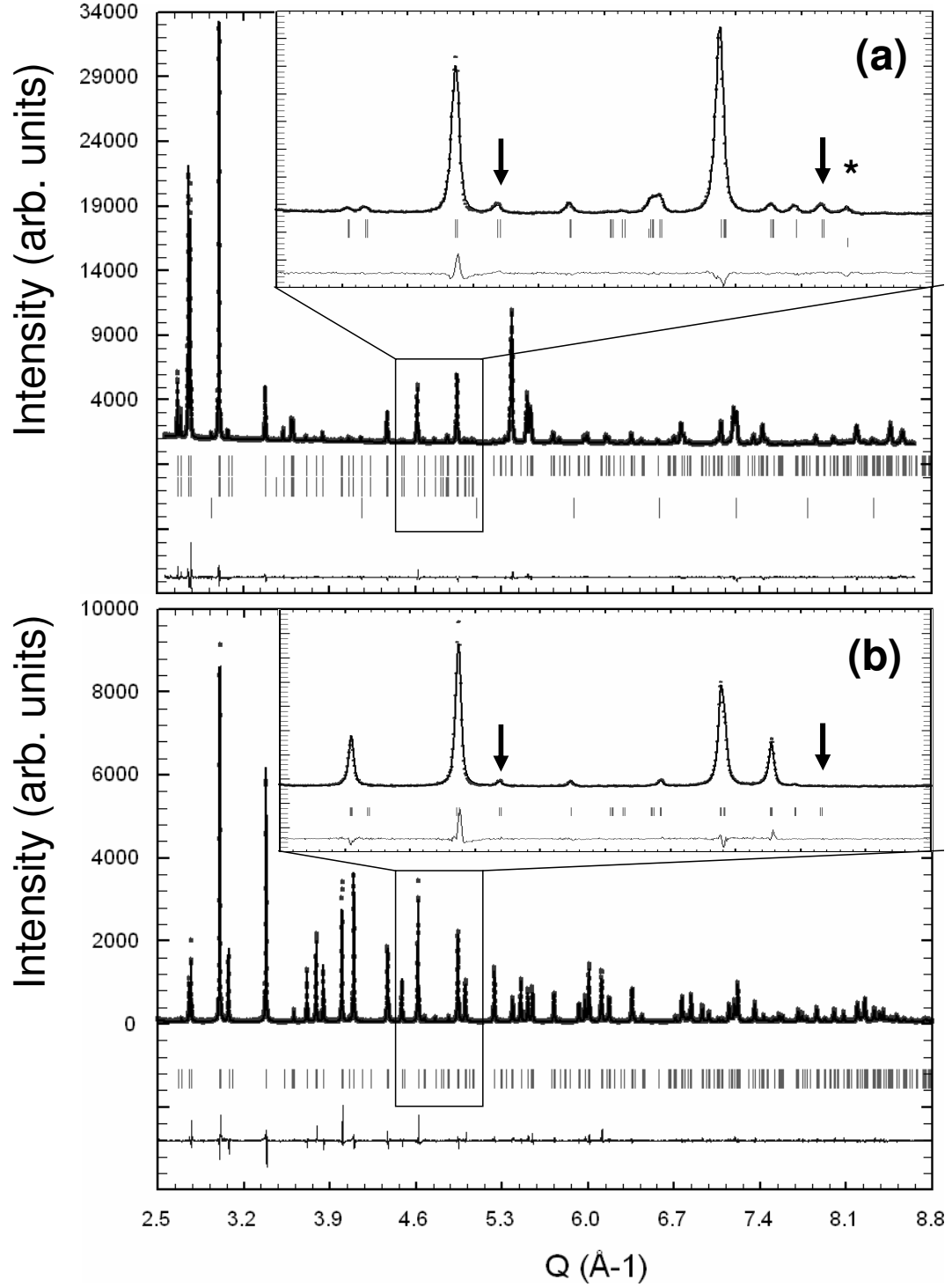


FIG. 4: Combined Rietveld refinement of the  $\text{SrMnO}_3$  structure at 100K with (a) NPD HRPD and (b) HR-SXPD ID-31 data collected on  $\text{SrMnO}_3$  at  $T = 100\text{K}$ . For both patterns, the continuous line correspond to the model fitting to the data, the lowest continuous line, the difference curve, and ticks are indicating the position of the Bragg reflections. For the NPD (a), the upper, middle and lower ticks represents the contribution from the nuclear scattering, the magnetic scattering, and the contribution from the Vanadium can (asterisk). Arrows indicate the position of the few reflections violating the extinction conditions of the high temperature space group  $P6_3/mmc$ .

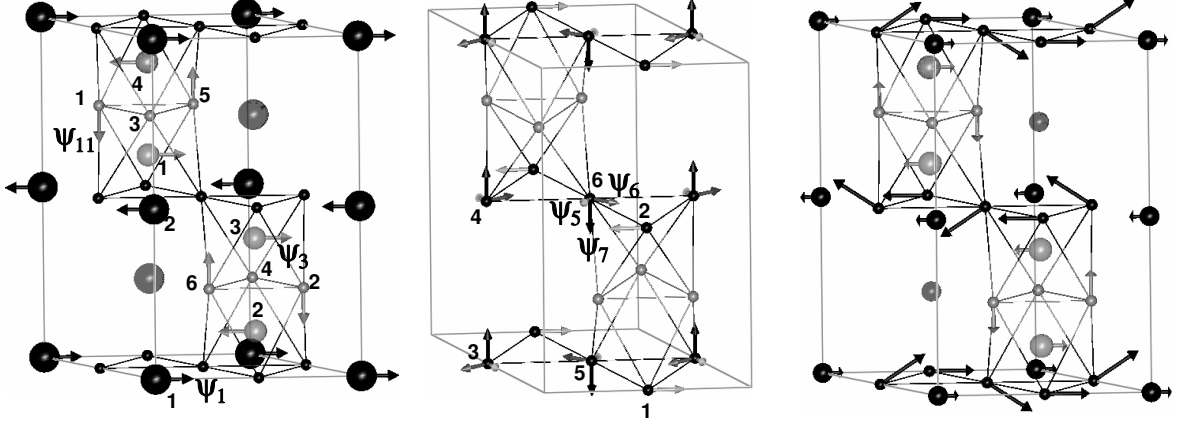


FIG .5: Atomic displacement modes responsible for the structural phase transition in  $\text{SrMnO}_3$ . The arrows and the atom labels gives a graphical representation of the basis vectors of Irrep.  $\Gamma_5$  involved in the transition, which are given table IV, Appendix A (a) Displacement modes for Mn (medium sized grey spheres),  $\text{Sr}_1$  (large black spheres) and  $\text{O}_2$  (small grey spheres) (b) Displacement modes for  $\text{O}_1$  (c) Resultant distortion from the linear combination  $\sum C_i \psi_i$  of all basis functions: the refinement leads to  $C_1 > 0$ ,  $C_3 < 0$  and  $C_{11} < 0$  for  $\text{Sr}_1$ , Mn, and  $\text{O}_2$  respectively For  $\text{O}_1$ , the mixing coefficients can be constrained to have no component along b, as  $C_5 = C_6 + C_7$



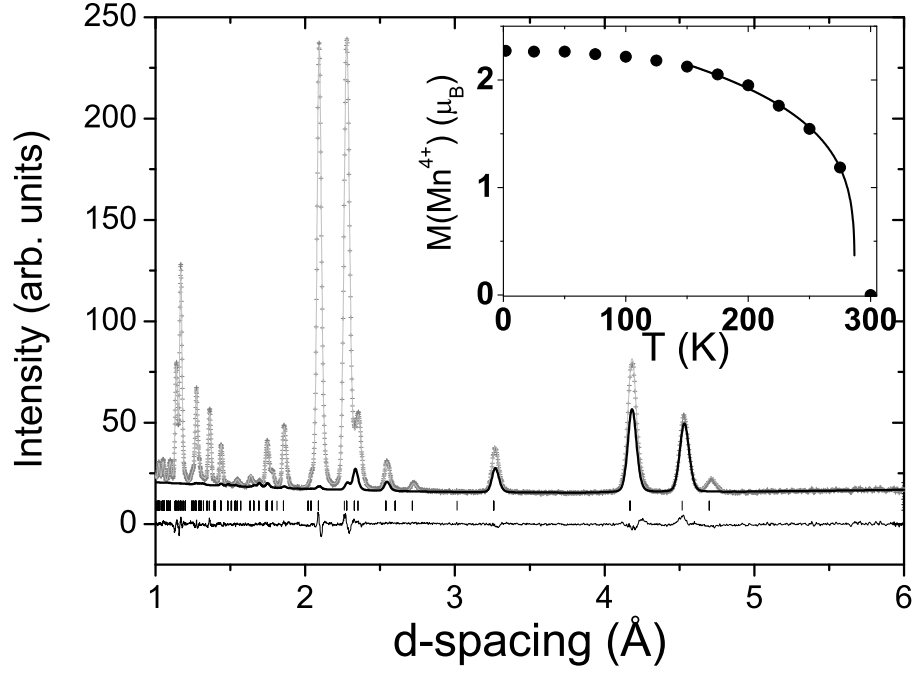


FIG. 6: Rietveld refinement of  $\text{SrMnO}_3$  at  $T = 1.5\text{K}$  with GEM data collected. Data from a detector bank situated at  $35^\circ 2'$  are shown. The experimental data points are shown as grey crosses while the calculated pattern is represented by a grey solid line. Contribution from magnetic scattering is plotted separately as a thick black solid line. The lowest continuous line shows the difference curve between data and refinement, while tick marks indicate the positions of Bragg reflections.

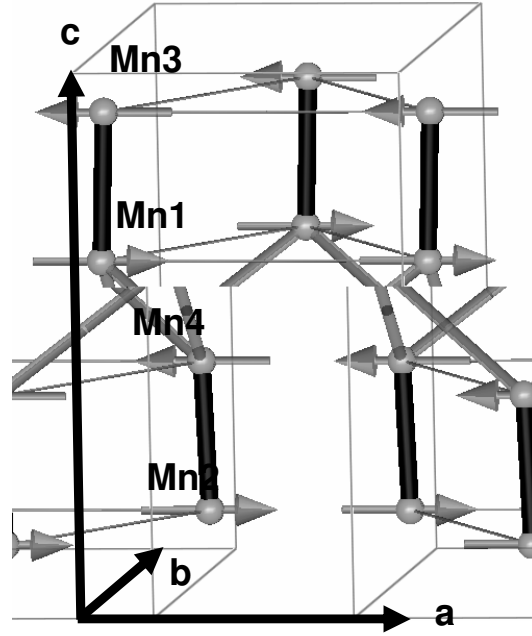


FIG . 7: Low temperature magnetic structure of  $\text{SrMnO}_3$ . It is described in the low temperature orthorhombic  $C222_1$  cell. The Mn atoms are labeled accordingly to the positions of the translated atoms given in Table V